Contents lists available at ScienceDirect

Results in Physics

An improved magnetic properties measurement scheme using a torsion pendulum

Binbin Liu [a,b], Zhen Yang [a], Li-e Qiang [a,*], Peng Xu [c,d,e], Xiaodong Peng [a,d,f,g], Ziren Luo [c], Yuzhu Zhang [a], Wenlin Tang [a]

[a] *National Space Science Center, Chinese Academy of Sciences, Beijing 100190, China*
[b] *School of Computer Science and Technology, University of Chinese Academy of Sciences, Beijing 100049, China*
[c] *Institute of Mechanics, Chinese Academy of Sciences, Beijing 100190, China*
[d] *Hangzhou Institute for Advanced Study, University of Chinese Academy of Sciences, Hangzhou 310024, China*
[e] *Lanzhou Center of Theoretical Physics, Lanzhou University, Lanzhou 730000, China*
[f] *Taiji Laboratory for Gravitational Wave Universe, Hangzhou Institute for Advanced Study, Hangzhou 310024, China*
[g] *Key Laboratory of Gravitational Wave Precision Measurement of Zhejiang Province, Hangzhou 310024, China*

ARTICLE INFO

ABSTRACT

Magnetic disturbance, originating arising from the interaction between the environmental magnetic field and the test mass (TM) properties, is a significant source of the high-precision inertial sensor noise in the space-borne gravitational wave detection missions, which puts forward an extremely stringent requirement on the TM magnetic cleanliness. Therefore, a torsion pendulum for on-ground testing is required to characterize the magnetic properties of a TM. We report an improved magnetic properties measurement scheme using a torsion pendulum with an electrostatically controlled block. In this novel scheme, four magnetometers are set near the TM for real-time monitoring the magnetic field, and a magnetic field correction method is proposed to improve the magnetic properties calculation precision. The results showed that the relative error of our method, compared with that of the traditional method, decreased from 35.40% to 2.38% for the component of the remnant magnetic moment m_y and from 8.65% to 6.75% for the magnetic susceptibility χ.

Introduction

An inertial sensor provides high-precision position sensing, which, combines with satellite drag-free control technology, shields the test mass (TM) from disturbance and ensures it falls freely in the gravitational field [1]. Therefore, inertial sensors are extensively used in microgravity experiments in space, such as Earth gravity field measurement [2–4], equivalence principle experiments [5–9], and space-based gravitational wave detection missions [1,10–12]. The primary performance metrics for an inertial sensor include its residual acceleration and low-frequency coverage [13]. For instance, for a space-borne gravitational wave detector, the residual acceleration noise of the TM is supposed to be below 3×10^{-15} ms^{-2} Hz$^{-1/2}$ from 0.1 mHz to 1 Hz [11]. To achieve such a high level of performance, all stray forces that may influence the TM movement should be analyzed and suppressed carefully [14]. Among them, the coupling force between the fluctuating magnetic field and TM magnetic properties, i.e., remanent magnetization **m** and susceptibility χ of TM, is a paramount contributor

to the total disturbance noise [11,15]. In the laser interferometer space antenna pathfinder (LISA Pathfinder) mission, for example, magnetic noise accounted for approximately 40% of the total noise budget [16]. The magnetic forces resulting from the coupling of the magnetic field and the magnetic properties can be mathematically expressed as follows (see Appendix for details)

$$\mathbf{F} = \iiint_{V_{\text{TM}}} \left[\left(\mathbf{m}_r + \frac{2\chi}{\mu_0} \mathbf{B} \right) \cdot \boldsymbol{\nabla} \right] \mathbf{B} \, dx \, dy \, dz, \tag{1}$$

where V_{TM} is the volume of the TM, $\mathbf{m}_r$ is the TM remanent magnetization per unit volume, μ_0 is the vacuum magnetic permeability, which is equal to $4\pi \times 10^{-7}$ mkg s^{-2}A^{-2}, **B** is the environmental magnetic field, and $dx\,dy\,dz$ is the volume element in the Cartesian coordinate system.

As both interplanetary and spacecraft magnetic fields can penetrate into the electrode housing and couple with the magnetic properties of TMs, TMs with low residual magnetic momentum and susceptibility are needed to suppress magnetic-related noise [17]. To meet the stringent

---

scientific requirements of LISA-like missions, the remanent magnetization and susceptibility of TMs are suggested to be $|\mathbf{m}| < 10\,\text{nA}\,\text{m}^2$ and $\chi < 3 \times 10^{-6}$, respectively [18]. Therefore, on-ground high-precision measurements of TM magnetic properties are required before spacecraft launch [17].

Traditional measurement instruments and methods, such as the physical property measurement system (PPMS), the Faraday method, and the Gouy method, are limited by the geometrical dimensions of materials and cannot be employed in the measurement of the magnetic properties of large centimeter-level TMs [19]. Consequently, innovative magnetic properties measurement devices were designed. Davis proposed a method based on a commercial electronic pendulum to measure the volume susceptibility of materials [20]. A superconducting quantum interference device (SQUID) was utilized to measure the magnetization of TM in the LISA Pathfinder mission [21]. The high-precision facility for weak force measurement, torsion pendulum, was used extensively to measure surface force/torque disturbances arising in the inertial sensor, including the magnetic properties of TM [22–25]. Hueller et al. proposed a torsion pendulum technique to accurately measure the magnetic properties of the LISA TM on the ground [17]. Tu et al. employed a torsion balance to test the magnetic properties of a titanium TM, and analyzed the factors that effect its sensitivity [26]. Xu et al. designed a torsion pendulum with a dual magnetic field modulation to measure the alternating current (ac) susceptibility of the TM from 50 μHz to 80 Hz and reached a resolution of 10^{-8} [27].

To solve the magnetic parameters of the TM from measured magnetic force/torque in torsion pendulum experiments, the magnetic field and its gradient acting on the TM must be precisely determined [22,26–32]. However, in these experiments, only the magnetic field generated by the coils was considered, which could be calculated from the coil parameters and currents, while the background magnetic field was generally ignored. This is feasible in magnetically clean conditions but will introduce a non-negligible bias in non-magnetically clean conditions. Yin et al. assessed the impact of the geomagnetic field and added two extra coils to counteract its effect; however, a deviation still exists [22]. Additionally, the contribution of magnetic fields from other magnetic sources around the torsion pendulum has not been considered.

In this study, we report a novel magnetic properties measurement scheme using a single-stage torsion pendulum; this scheme can be used to specifically deal with the incomplete magnetic cleanliness in the surrounding environment and greatly improve the calculation precision. The rest of this paper is organized as follows. In Section "Method", the entire measurement principle and magnetic field correction method based on the torsion pendulum are introduced, and Section "Experiment" describes the torsion pendulum and experimental design. The simulated results and noise analysis are detailed in Section "Results and discussion". Finally, the conclusions of the study are presented in Section "Conclusion".

Method

Magnetic properties measurement principle

The TM magnetic properties ($\mathbf{m}$ and χ) can be calculated from the measured magnetic torque acted on the TM [22]. One of the high-precision instruments for torque measurement is the single-stage torsion pendulum, as shown in Fig. 1. The suspended TM is located in the electrode cage between two circular energized coils, which generate the applied magnetic field. Four magnetometers are installed at the surface of the electrode cage, and their readouts are used to correct the magnetic field around TM. The center of the TM is chosen as the origin, the x-axis is set parallel to the fiber, and the z-axis is perpendicular to the plane of the coils, extending from the plane of coil 2 to the plane of coil 1. The y-axis complies with the right-hand rule of the Cartesian coordinate system. The magnetic torque exerted on the TM produced by the energized coils is balanced by the electrostatic torque generated by
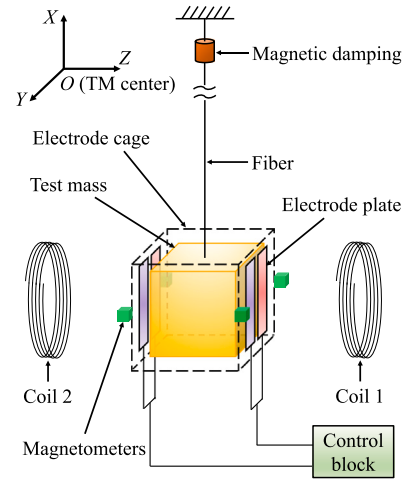

Fig. 1. Schematic view of a single-stage torsion pendulum.

the electrode plates. The detected x-component of the magnetic torque N_{m} satisfy

$$\left(N_{\text{m}}\right)_x + \left(N_{\text{e}}\right)_x = 0, \tag{2}$$

where $\left(N_{\text{e}}\right)_x$ is the x component of the electrostatic torque obtained by the control block readout.

The magnetic torque exerted on the TM could be expressed as

$$\begin{aligned}\left(N_{\text{m}}\right)_x &= \iiint_{V_{\text{TM}}} \left(\mathbf{r} \times \mathbf{f} + \mathbf{m}_{\text{r}} \times \mathbf{B}\right)_x dx\,dy\,dz \\ &= \iiint_{V_{\text{TM}}} \left[\left(yf_z - zf_y\right) \right. \\ &\quad \left. + \left(m_{\text{r,y}}B_z - m_{\text{r,z}}B_y\right)\right] dx\,dy\,dz, \end{aligned} \tag{3}$$

where $\mathbf{r}$ is the position vector relative to the origin, $m_{\text{r,y}}$ and $m_{\text{r,z}}$ are the y and z components of the $\mathbf{m}_{\text{r}}$, respectively. $\mathbf{f}$ is the magnetic force per unit volume, and its two components f_y and f_z can be expressed as

$$f_y = \left(\mathbf{m}_{\text{r}} + \frac{2\chi}{\mu_0}\mathbf{B}\right) \cdot \frac{\partial \mathbf{B}}{\partial y}, \tag{4}$$

$$f_z = \left(\mathbf{m}_{\text{r}} + \frac{2\chi}{\mu_0}\mathbf{B}\right) \cdot \frac{\partial \mathbf{B}}{\partial z}. \tag{5}$$

Following Eq. (2) and together with the assumption of a uniform distribution of remnant magnetic moment within TM, Eq. (3) can be further expressed as

$$\begin{aligned}-\left(N_{\text{e}}\right)_x &= \iiint_{V_{\text{TM}}} \left[\left(\frac{m_y}{V_{\text{TM}}} + \frac{2\chi}{\mu_0}B_y\right)\left(y\frac{\partial B_y}{\partial z} - z\frac{\partial B_y}{\partial y}\right)\right. \\ &\quad + \left(\frac{m_z}{V_{\text{TM}}} + \frac{2\chi}{\mu_0}B_z\right)\left(y\frac{\partial B_z}{\partial z} - z\frac{\partial B_z}{\partial y}\right) \\ &\quad \left. + \left(\frac{m_y}{V_{\text{TM}}}B_z - \frac{m_z}{V_{\text{TM}}}B_y\right)\right] dx\,dy\,dz, \end{aligned} \tag{6}$$

where m_y and m_z are the components of the TM remnant magnetic moment $\mathbf{m}$ to be solved. B_y and B_z are the components of the magnetic field, while $\partial B_y/\partial y$, $\partial B_y/\partial z$, $\partial B_z/\partial y$, and $\partial B_z/\partial z$ are the components of the magnetic field gradient, respectively. The term

$$\iiint_{V_{\text{TM}}} \left(\frac{m_x}{V_{\text{TM}}} + \frac{2\chi}{\mu_0}B_x\right)\left(y\frac{\partial B_x}{\partial z} - z\frac{\partial B_x}{\partial y}\right) dx\,dy\,dz \tag{7}$$

is ignored in Eq. (6), since the y and z components of ∇B_x have an average of zero owing to the symmetry of the coils magnetic field.

To solve the three magnetic properties m_y, m_z and χ in Eq. (6), at least three sets of independent electrostatic torque measurement experiments data are required, and the torque measured in the kth
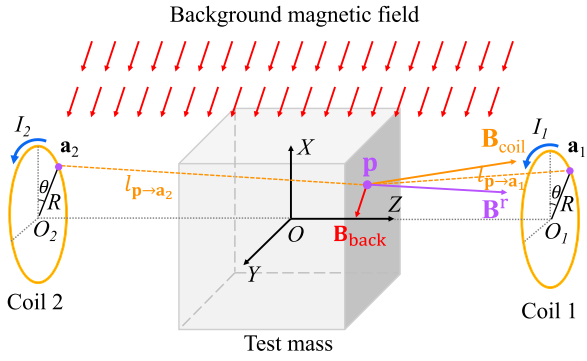
Fig. 2. Simplified schematic view of the calculation of magnetic field **B** at point **p** in the presence of background magnetic field.

Fig. 3. The magnetic properties calculation processing using the traditional and magnetic field correction methods.

experiment can be cast in the form:

$$- \left(N_e^{(k)} \right)_x = m_y \, \mathcal{F}(\mathbf{B}^{(k)}) + m_z \, \mathcal{G}(\mathbf{B}^{(k)}) + \chi \, \mathcal{H}(\mathbf{B}^{(k)}), \tag{8}$$

where $k = 1, 2, 3$ is the order of experiments, and

$$\mathcal{F}(\mathbf{B}^{(k)}) = \frac{1}{V_{\text{TM}}} \iiint_{V_{\text{TM}}} \left(y \frac{\partial B_y^{(k)}}{\partial z} - z \frac{\partial B_y^{(k)}}{\partial y} + B_z^{(k)} \right) dx \, dy \, dz, \tag{9}$$

$$\mathcal{G}(\mathbf{B}^{(k)}) = \frac{1}{V_{\text{TM}}} \iiint_{V_{\text{TM}}} \left(y \frac{\partial B_z^{(k)}}{\partial z} - z \frac{\partial B_z^{(k)}}{\partial y} - B_y^{(k)} \right) dx \, dy \, dz, \tag{10}$$

$$\mathcal{H}(\mathbf{B}^{(k)}) = \frac{2}{\mu_0} \iiint_{V_{\text{TM}}} \left[B_y^{(k)} \left(y \frac{\partial B_y^{(k)}}{\partial z} - z \frac{\partial B_y^{(k)}}{\partial y} \right) \right.$$
$$\left. + B_z^{(k)} \left(y \frac{\partial B_z^{(k)}}{\partial z} - z \frac{\partial B_z^{(k)}}{\partial y} \right) \right] dx \, dy \, dz, \tag{11}$$

are coefficients of the TM magnetic properties m_y, m_z and χ, respectively. Finally, two components of the TM remnant magnetic moment (m_y, m_z), and the magnetic susceptibility (χ) are obtained by solving the Eqs. (8). By adjusting the orientation of the TM, another component of the TM remnant magnetic moment (m_x) can also be measured using this method [26].

According to Eq. (8), the calculation accuracy of the magnetic properties is primarily affected by the accuracy of the measured torque $(N_e^{(k)})_x$, and the three coefficients of magnetic properties, namely $\mathcal{F}(\mathbf{B}^{(k)})$, $\mathcal{G}(\mathbf{B}^{(k)})$ and $\mathcal{H}(\mathbf{B}^{(k)})$. Therefore, the accuracy of the magnetic field **B** should be high enough to ensure the TM magnetic properties calculation precision.

In fact, the magnetic field exerted on TM includes the magnetic field generated by the coils and the background magnetic field, as shown in Fig. 2. In traditional method, the background magnetic field is ignored, and the real magnetic field in Eqs. (8)–(11) is approximated by the coils magnetic field, which leads to an error in the TM magnetic properties solution. Herein, a magnetic field correction method (see Section "Magnetic field correction method") was proposed to reduce the error of the TM magnetic properties by adopting a corrected magnetic field as the estimation of magnetic field.

The entire magnetic properties calculation processing using the traditional and magnetic field correction methods are summarized in Fig. 3. In the traditional method, the coils magnetic field and the measured magnetic torque are used to calculate the magnetic properties directly. However, in the magnetic field correction method, four magnetometers are added in the torsion pendulum, and their readout, together with the coils magnetic field, are employed to generate the corrected magnetic field. Using the corrected magnetic field and the measured magnetic torque, the magnetic properties can be calculated.
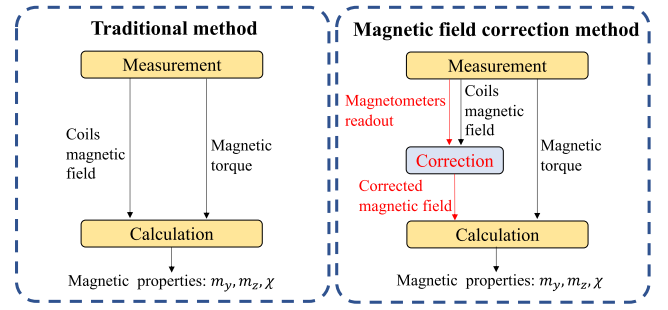
Magnetic field correction method

The real magnetic field at an arbitrary point $\mathbf{p}(x_p, y_p, z_p)$ inside TM in Fig. 2 can be expressed as

$$\mathbf{B}^r(\mathbf{p}) = \mathbf{B}_{\text{coil}}(\mathbf{p}) + \mathbf{B}_{\text{back}}(\mathbf{p}), \tag{12}$$

where $\mathbf{B}_{\text{coil}}(\mathbf{p})$ is the magnetic field generated by the two coils, and $\mathbf{B}_{\text{back}}(\mathbf{p})$ is the background magnetic field.

According to the Biot–Savart law, the coils magnetic field $\mathbf{B}_{\text{coil}}(\mathbf{p})$ can be expressed as [33]

$$\mathbf{B}_{\text{coil}}(\mathbf{p}) = \frac{\mu_0 N}{4\pi} \cdot$$
$$\left\{ \left[\int_0^{2\pi} R \cos\theta \sum_{i=1}^{2} \frac{I_i \left(z_p - z_{oi} \right)}{|l_{\mathbf{p} \to \mathbf{a}_i}|^3} d\theta \right] \mathbf{i} \right.$$
$$+ \left[\int_0^{2\pi} R \sin\theta \sum_{i=1}^{2} \frac{I_i \left(z_p - z_{oi} \right)}{|l_{\mathbf{p} \to \mathbf{a}_i}|^3} d\theta \right] \mathbf{j}$$
$$\left. + \left[\int_0^{2\pi} R \sum_{i=1}^{2} \frac{I_i \left(\sin\theta \left(y_{oi} - y_p \right) + R - \cos\theta x_p \right)}{|l_{\mathbf{p} \to \mathbf{a}_i}|^3} d\theta \right] \mathbf{k} \right\}, \tag{13}$$

where $\mathbf{i} = (1, 0, 0)^T$, $\mathbf{j} = (0, 1, 0)^T$, $\mathbf{k} = (0, 0, 1)^T$ are the unit base vectors, N is the number of coils turns, R is the radius of the two coils; $I_{1(2)}$ and $O_{1(2)} \left(x_{o1(2)}, y_{o1(2)}, z_{o1(2)} \right)$ are the current and center of coil 1(2), respectively; θ is the integral variable that represents the angle between the vector from O_i to the point $\mathbf{a}_i(R \cos\theta, R \sin\theta + y_{oi}, z_{oi})$ and the positive direction of the x-axis, as shown in Fig. 2; and $|l_{\mathbf{p} \to \mathbf{a}_i}| = |\mathbf{p} - \mathbf{a}_i|$ is the distance between **p** and the point $\mathbf{a}_i$ on the energized coil i, with $i = 1, 2$.

The background magnetic field $\mathbf{B}_{\text{back}}(\mathbf{p})$ can be estimated by the multipole expansion method. Since the background magnetic field in the TM region satisfy $\nabla \times \mathbf{B}_{\text{back}} = \nabla \cdot \mathbf{B}_{\text{back}} = 0$, $\mathbf{B}_{\text{back}}(\mathbf{p})$ can be expressed as [33]

$$\mathbf{B}_{\text{back}}(\mathbf{p}) = \sum_{l=1}^{\infty} \sum_{m=-l}^{l} M_{lm} \nabla \left[r^l Y_{lm}(\theta, \varphi) \right], \tag{14}$$

where (r, θ, φ) is the spherical coordinate of **p**; Y_{lm} is the standard spherical harmonic function, and M_{lm} is the multipole coefficient of degree l and order m, which can be solved by the boundary conditions. The multipole expansion is truncated after degree $l = L$, since the number of magnetometers N_{mag} near TM is limited. Then, the estimated background magnetic field can be expressed as

$$\mathbf{B}_{\text{back}}^e(\mathbf{p}) = \sum_{l=1}^{L} \sum_{m=-l}^{l} M_{lm} \nabla \left[r^l Y_{lm}(\theta, \varphi) \right]. \tag{15}$$

To obtain the best estimation of the M_{lm}, a least-squares method is employed to minimize the equation $\partial \varepsilon^2 / \partial M_{lm} = 0$. Herein, the square
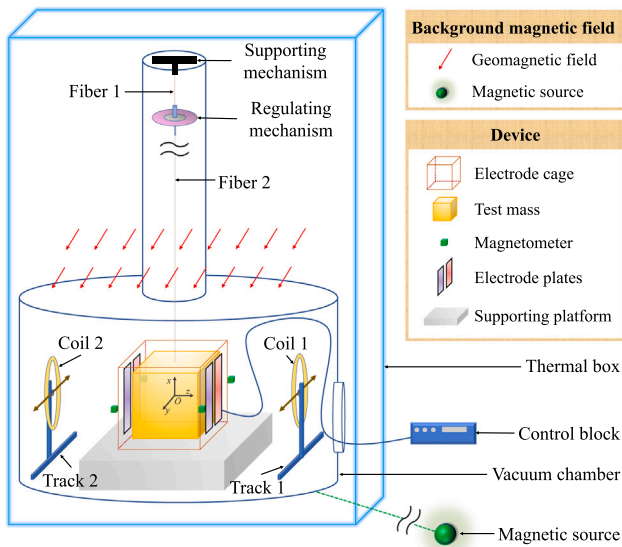
Fig. 4. Schematic diagram of a torsion pendulum in the presence of background magnetic field.

error is given by

$$\epsilon^2 \left(M_{lm} \right) = \sum_{s=1}^{N_{\mathrm{mag}}} \left| \mathbf{B}_{\mathrm{back}} \left(\mathbf{x}_s \right) - \mathbf{B}_{\mathrm{back}}^{\mathrm{e}} \left(\mathbf{x}_s \right) \right|^2$$

$$= \sum_{s=1}^{N_{\mathrm{mag}}} \left| \left[\mathbf{B}_{\mathrm{read}} \left(\mathbf{x}_s \right) - \mathbf{B}_{\mathrm{coil}} \left(\mathbf{x}_s \right) \right] - \mathbf{B}_{\mathrm{back}}^{\mathrm{e}} \left(\mathbf{x}_s \right) \right|^2, \quad (16)$$

where $\mathbf{B}_{\mathrm{back}} \left(\mathbf{x}_s \right)$ is the background magnetic field at the sth magnetometers $\mathbf{x}_s$, $\mathbf{B}_{\mathrm{read}} \left(\mathbf{x}_s \right)$ is the readout of the sth magnetometer ($s = 1, 2, \ldots, N_{\mathrm{mag}}$). Once the system of equations is solved, the optimal coefficients M_{lm} are replaced back into Eq. (15) and then the estimated background magnetic field at point $\mathbf{p}$ could be subsequently obtained.

Finally, the corrected magnetic field can be calculated by

$$\mathbf{B}_{\mathrm{correction}} \left(\mathbf{p} \right) = \mathbf{B}_{\mathrm{coil}} \left(\mathbf{p} \right) + \mathbf{B}_{\mathrm{back}}^{\mathrm{e}} \left(\mathbf{p} \right). \quad (17)$$

Experiment

Description of torsion pendulum

A schematic of the single-stage torsion pendulum is illustrated in Fig. 4. Fiber 1 connects the top supporting mechanism with the magnetic damper regulating mechanism, which aims to reduce the TM oscillation. The cubical-shaped Au-Pt alloy TM, with dimensions of $46 \times 46 \times 46$ mm^3, is suspended by fiber 2 and located between two energized circular coils with an equivalent radius R of 20 mm. Both coils are located (75 ± 1) mm away from the origin along the z-axis, and the total number of turns N for each coil is 300. The coils could move along the tracks parallel to the y-axis, and the magnitudes and directions of currents in the coils can also be adjusted. The energized coils in various configurations will generate different magnetic torques exerted on the TM. The TM is located in the electrode cage, which is installed on the supporting platform. Within the electrode cage, two pairs of electrode plates are set perpendicular to the z-axis, and they are connected with a control block to obtain the feedback voltage of the electrode plate. In the experiment, there is no magnetic shield instrument in the torsion pendulum. To improve the sensitivity by keeping the thermal noise low, the entire instrument is operated in a high vacuum chamber, which is installed within a thermal box at 293.15 K aiming to reduce the torque noise induced by temperature fluctuations [30,32].
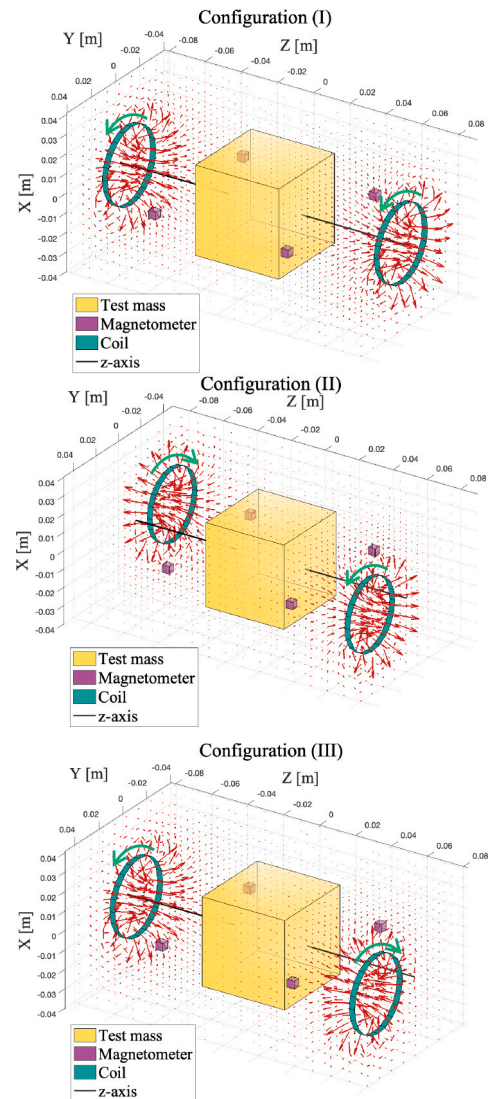

Fig. 5. Magnetic fields produced by the coils in the three configurations. The red arrows represent the coils magnetic fields around the TM, and the current directions of the coils are indicated by green arrows. The interpretations of the test mass, magnetometer and coil are listed in the legend. (For interpretation of the references to color in this figure legend, the reader is referred to the web version of this article.)

Table 1
Different coils configurations.

Configuration	I_1 (A)	I_2 (A)	y_{o1} (mm)	y_{o2} (mm)
(I)	1.2 ± 0.001	1.2 ± 0.001	0 ± 0.05	0 ± 0.05
(II)	1.2 ± 0.001	-1.2 ± 0.001	25 ± 0.05	-25 ± 0.05
(III)	-1.2 ± 0.001	1.2 ± 0.001	25 ± 0.05	0 ± 0.05

Experimental design

Coils configurations and coils magnetic fields: The TM magnetic properties can be obtained by developing at least three torque measurement experiments, as mentioned in Section "Magnetic properties measurement principle". The positions and currents of the coils should be carefully designed to obtain three independent sets of magnetic properties coefficients, $\mathcal{F}(\mathbf{B}^{(k)})$, $\mathcal{G}(\mathbf{B}^{(k)})$, and $\mathcal{H}(\mathbf{B}^{(k)})$. In our experiment, the coils configurations are listed in Table 1, and the magnetic fields generated by the coils are depicted in Fig. 5. In configuration (I), coils 1 and 2 were symmetrically installed relative to the $x - o - y$ plane and had the same current direction. The two coils were installed
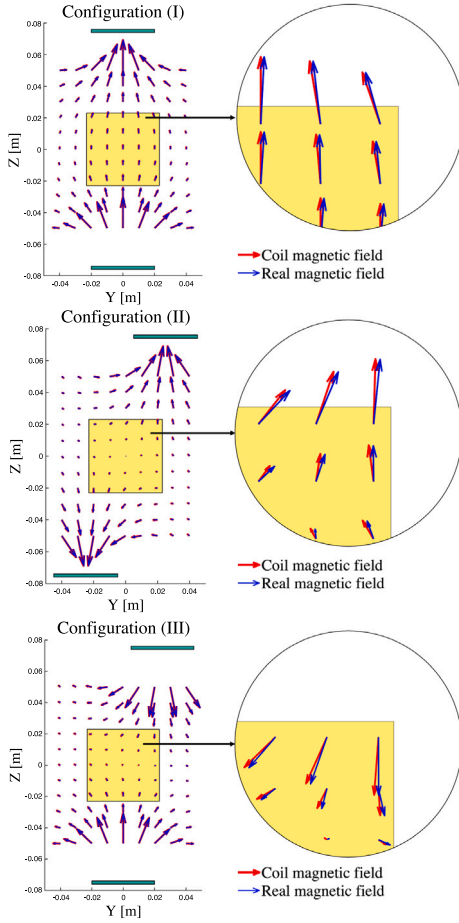
Fig. 6. Comparison between the coil and real magnetic fields. The real magnetic field comprises the coil magnetic field, the geomagnetic field and the field generated by one magnetic dipole. The red and blue arrows represent the projections of the coils and real magnetic fields in the $x = 0$ plane, respectively. (For interpretation of the references to color in this figure legend, the reader is referred to the web version of this article.)
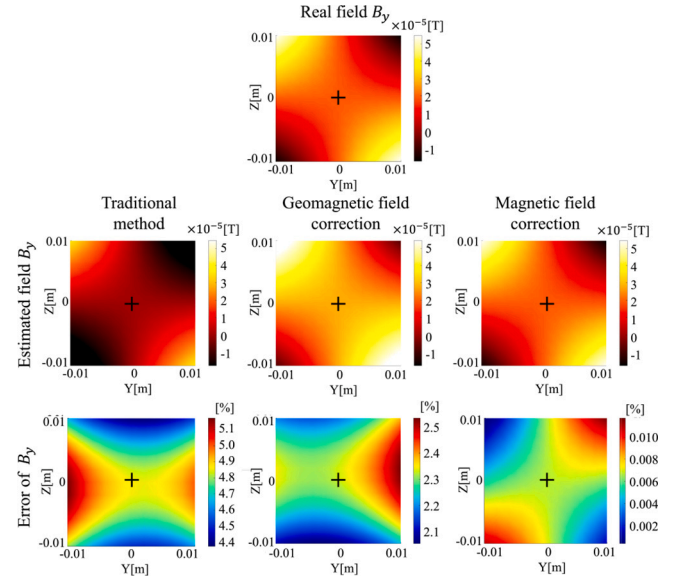

Fig. 7. Contour plot of the real magnetic field (top panel), estimated magnetic fields (middle panel) and relative errors (bottom panel) using three methods. Herein, the traditional, the geomagnetic field correction and the magnetic correction methods are employed. The relative error is defined as $\varepsilon_{B_y} = |(\mathbf{B}^r - \mathbf{B}^e)_y / |\mathbf{B}^r||$. The background magnetic field includes the geomagnetic field and one magnetic dipole of $\rho = 10\,\mathrm{Am}^2$ in modulus. The black '+' represents the TM center. Note the same scale for the field bars, while different scale for the error bars.

centrosymmetrically with opposite current directions in configuration (II), whereas in configuration (III), they were respectively located at $(0, 75 \pm 1, 25 \pm 0.05)$ mm and $(0, -75 \pm 1, 0 \pm 0.05)$ mm with I_1, I_2 running in opposite current directions.

Background magnetic field: In the experiment, two types of background magnetic fields were considered: one is the geomagnetic field; the other is the magnetic field generated by the unknown magnetic sources. The real magnetic field, taking the background magnetic field into consideration, deviates slightly from the coils magnetic field, as shown in Fig. 6.

Generally, the magnitude of the geomagnetic field is approximately $25\,000$–$65\,000$ nT, and the local geomagnetic field can be obtained by querying the World Magnetic Model [34]. For example, in the Cartesian coordinate system shown in Fig. 2, the geomagnetic field components of Beijing (40° N, 117° E, 43 m above sea level) can be written as

$$\mathbf{B}_{\mathrm{geo}} = (-47101.8, 27757.6, -3720.9)\ \mathrm{nT}. \tag{18}$$

General speaking, an unknown magnetic source can be regarded as single or multiple magnetic dipoles, then the magnetic field produced by the unknown sources can be expressed as

$$\mathbf{B}_{\mathrm{dipole}}(\mathbf{p}) = \frac{\mu_0}{4\pi} \sum_{a=1}^{N_d} \frac{3\left[\mathbf{m}_a \cdot \mathbf{n}_a\right]\mathbf{n}_a - \mathbf{m}_a}{|\mathbf{p} - \mathbf{x}_a|^3}, \tag{19}$$

where N_d is the total number of dipoles, $\mathbf{m}_a$ is the magnetic moment of the ath magnetic dipole with position $\mathbf{x}_a$, and $\mathbf{n}_a = (\mathbf{p} - \mathbf{x}_a)/|\mathbf{p} - \mathbf{x}_a|$ is

a unit vector from the ath dipole position to the point $\mathbf{p}$. Without loss of generality, a single magnetic dipole was considered to represent the unknown magnetic source in this experiment. The dipole was located at $(30 \pm 0.1, 30 \pm 0.1, 30 \pm 0.1)$ cm with a fixed modulus, whereas the dipole orientation was selected randomly.

Magnetometers: Some miniaturized magnetic sensors, such as the giant magneto-impedance [35], anisotropic magnetoresistance [36–38], and tunneling magnetoresistance [39], are recommended for close monitoring of the magnetic field around TM. Herein, four anisotropic magnetoresistance sensors were used in the magnetic field correction method. They were symmetrically installed with positions of $(0 \pm 1, 36.5 \pm 1, 36.5 \pm 1)$ mm, $(0 \pm 1, 36.5 \pm 1, -36.5 \pm 1)$ mm, $(0 \pm 1, -36.5 \pm 1, 36.5 \pm 1)$ mm, and $(0 \pm 1, -36.5 \pm 1, -36.5 \pm 1)$ mm, respectively.

Results and discussion

Magnetic field correction

In the experiment, the accuracy of the magnetic field affected the calculation precision of the TM magnetic properties. Herein, three methods, including the traditional method, geomagnetic field correction method,[1] and magnetic field correction method, are employed. The estimated magnetic field components B_y obtained through these three methods are presented in Fig. 7, and the corresponding estimation errors are also graphically displayed. As can be observed, the traditional method exhibits unsatisfactory magnetic field estimation, with a relative error of over 4.8% at the TM center. The geomagnetic field correction method provides superior magnetic field estimation compared to the traditional method, but its TM center error still exceeds 2.3%. However, the magnetic field correction method offers a reliable magnetic field estimation with a relative error below 0.01% at the TM center.

---

[1] In the geomagnetic field correction method, the total magnetic field includes the coils magnetic fields and the geomagnetic field (the unknown magnetic source is not considered).
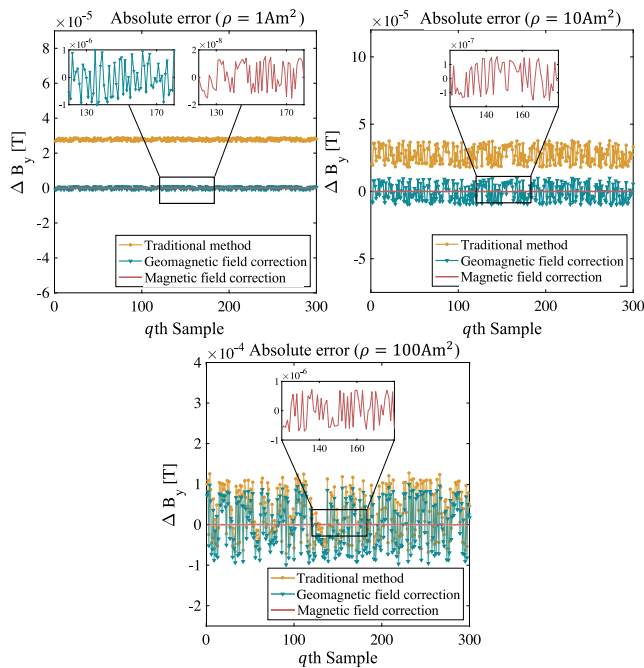
Fig. 8. The absolute error of B_y relative to the qth ($q = 1, \dots, 300$) random dipole orientation sample under three dipole moments $\rho = 1, 10, 100 \, \text{Am}^2$. The traditional method (yellow line with dots), geomagnetic field correction method (green line with triangle), and magnetic field correction method (red line) are employed. (For interpretation of the references to color in this figure legend, the reader is referred to the web version of this article.)
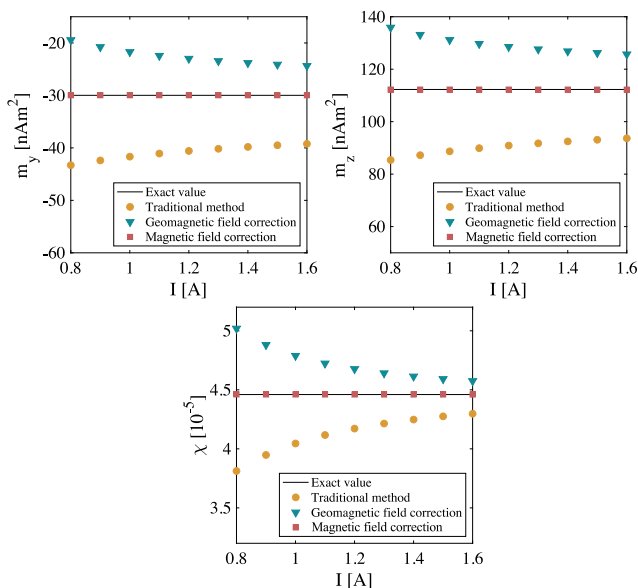

Fig. 9. The TM magnetic properties (m_y, m_z, and χ) calculated by the traditional method (yellow circles), geomagnetic field correction method (green triangles), and magnetic field correction method (red squares) as a function of the coils currents. The exact values (black lines) of magnetic properties are also presented. The background magnetic field includes the geomagnetic field and one magnetic dipole of $\rho = 10 \, \text{Am}^2$ in modulus. (For interpretation of the references to color in this figure legend, the reader is referred to the web version of this article.)

To study the magnetic field precision of the three methods under different magnetic environments, 300 sets of dipole orientation samples were randomly selected under three moment moduli $\rho = 1, 10, 100 \, \text{Am}^2$, respectively. The absolute error of the estimated magnetic field is

Table 2
TM magnetic properties calculation results and relative errors.

TM magnetic properties	m_y		m_z		χ	
	Value [nA m²]	Error [%]	Value [nA m²]	Error [%]	Value [10^{-6}]	Error [%]
Exact value	−29.98	–	112.27	–	44.60	–
Traditional method	−40.58	35.37	90.89	19.04	41.72	6.46
Geomagnetic field correction	−22.99	23.32	128.53	14.49	46.77	4.86
Magnetic field correction	−29.96	**0.07**	112.22	**0.05**	44.61	**0.01**

defined to characterize the difference between the real and estimated magnetic fields as

$$\Delta \mathbf{B} = \mathbf{B}^\text{r} - \mathbf{B}^\text{e}, \tag{20}$$

where $\mathbf{B}^\text{r} = \mathbf{B}_\text{coil} + \mathbf{B}_\text{geo} + \mathbf{B}_\text{dipole}$ is the real magnetic field, $\mathbf{B}^\text{e}$ is the estimated magnetic field. For traditional method, $\mathbf{B}^\text{e} = \mathbf{B}_\text{coil}$; for geomagnetic field correction method, $\mathbf{B}^\text{e} = \mathbf{B}_\text{coil} + \mathbf{B}_\text{geo}$; for magnetic field correction method, $\mathbf{B}^\text{e} = \mathbf{B}_\text{correction}$. Fig. 8 shows that, as the dipole modulus grows from $1 \, \text{Am}^2$ to $10 \, \text{Am}^2$ and then to $100 \, \text{Am}^2$, the absolute errors of B_y increase for all three methods. Apparently, the absolute error ΔB_y of the magnetic field correction method is almost two magnitude orders lower than that of the traditional and geomagnetic field correction methods.

Magnetic properties calculation

Based on the experimental design explained in Section "Experimental design", the results and errors of the TM magnetic properties calculation are listed in Table 2. In the experiment, the *priori* exact values of the TM magnetic properties are given by $m_y = -29.98 \, \text{nAm}^2$, $m_z = 112.27 \, \text{nAm}^2$, and $\chi = 4.46 \times 10^{-5}$, respectively. The background magnetic field comprises the geomagnetic field and a magnetic dipole with a moment modulus of $\rho = 10 \, \text{Am}^2$. As can be observed, both the traditional and geomagnetic field calculation methods exhibit larger calculation errors than the magnetic field correction method. This confirms the effectiveness of magnetic field correction in improving the calculation accuracy.

Fig. 9 displays the TM magnetic properties solved by the three methods as a function of the coils currents (from 0.8 A to 1.6 A). The traditional method exhibits the largest calculation error, while the geomagnetic field correction method yields smaller errors in comparison. In contrast, the magnetic properties calculated by the magnetic field correction method closely align with the exact values. Particularly, the magnetic field correction method maintains high precision even as the coils currents weaken, while the accuracy of the other two methods decreases. This experiment indicates that the magnetic field correction method can effectively reduce errors caused by ignoring the influence of the background magnetic field, and provide a more accurate TM magnetic properties calculation in case of weak applied magnetic field.

Noise analysis

Besides the method error (see Table 2), the magnetic properties calculation precision is also disturbed by the errors induced by the experimental devices, such as the torsion pendulum, coils and magnetometers. Table 3 lists the magnetic properties calculation errors of each source using the traditional and magnetic field correction methods. Herein, the geomagnetic field and one dipole with moment modulus $\rho = 10 \, \text{Am}^2$ composed of the background magnetic field. Line 1 lists the errors caused by the methods. Lines 2–5 and lines 6–8 list the errors induced by the torsion pendulum and coils, respectively. Lines 9–11 only list the errors induced by the magnetometers for the magnetic field correction method, since the magnetometers were not used in the traditional method. Line 12 lists the total error of the two methods by calculating the quadratic sum of each error term.

Table 3

The magnetic properties calculation errors using the traditional method and magnetic field correction method in the presence of background magnetic field.

Line	Error source	Error term	Error value	Traditional method				Magnetic field correction method			
				Error of m_y		Error of χ		Error of m_y		Error of χ	
				$[\mathrm{nA\,m^2}]$	[%]	$[10^{-6}]$	[%]	$[\mathrm{nA\,m^2}]$	[%]	$[10^{-6}]$	[%]
1	Method	Method error	–	10.60	35.37	2.88	6.46	**0.02**	**0.07**	**0.01**	**0.01**
2	Torsion pendulum	Accuracy of capacitive sensor C_n	$2 \times 10^{-7}\mathrm{pF\,Hz^{-1/2}}$ [40]	5.97e−5	1.99e−4	6.50e−5	1.46e−4	5.97e−5	1.99e−4	6.50e−5	1.46e−4
3	Torsion pendulum	Readout noise V_{fn}	$2\,\mathrm{\mu V\,Hz^{-1/2}}$ [41]	1.88e−4	6.28e−4	3.04e−4	6.81e−4	1.88e−4	6.28e−4	3.04e−4	6.81e−4
4	Torsion pendulum	Thermal noise of fiber τ_{th}	$5 \times 10^{-14}\mathrm{Nm\,Hz^{-1/2}}$ [22]	5.28e−5	1.76e−4	5.47e−5	1.23e−4	5.28e−5	1.76e−4	5.47e−5	1.23e−4
5	Torsion pendulum	Calibration error of actuator	<1% [22]	0.30	1.00	0.45	1.00	0.30	1.00	0.45	1.00
6	Coil	Installation error (z-axis)	<1 mm [42]	0.36	1.20	2.53	5.67	0.36	1.20	2.53	5.67
7	Coil	Installation error (y-axis)	<50 μm [22]	0.20	0.67	0.02	0.05	0.20	0.67	0.02	0.05
8	Coil	Stability of currents I_1, I_2	<1 mA [22]	0.03	0.08	0.03	0.06	0.03	0.08	0.03	0.06
9	Magnetometers	Installation error	<1 mm [42]	–	–	–	–	0.49	1.62	1.57	3.51
10	Magnetometers	Offset error	<10 nT [42]	–	–	–	–	0.03	0.10	0.01	0.02
11	Magnetometers	Orthogonality of axes	<0.2° [43]	–	–	–	–	0.09	0.31	0.02	0.06
12	–	**Total error**	–	10.61	35.40	3.86	8.65	**0.71**	**2.38**	**3.01**	**6.75**

As shown in Table 3, the magnetic properties calculation method errors using the traditional method are 35.37% for m_y and 6.46% for χ, whereas those using the magnetic field correction method are clearly suppressed to below 0.1%. Both methods exhibit same errors induced by the torsion pendulum and coil, with the largest errors stemming from the coil installation (z-axis). For the magnetic field correction method, the installation error of the magnetometers also introduced a large error, so the magnetometers should be installed carefully. In terms of the total error, the reduction effects of the magnetic field correction method relative to the traditional method are from 35.40% to 2.38% for m_y and from 8.65% to 6.75% for χ, which are not as significant as the method error reduction effects. This is primarily limited by the coils and magnetometers installation errors, as shown in lines 6 and 9 of Table 3.

Conclusion

Space-based gravitational wave detection puts forward strict requirements for the TM magnetic properties ($\mathbf{m}$ and χ), which need to be accurately measured using an on-ground torsion pendulum. However, the inaccuracy of magnetic field estimation will introduce an error to the magnetic properties calculation. In this paper, a magnetic properties measurement scheme was proposed to improve the calculation precision of TM magnetic properties. Four magnetometers were installed around the TM to monitor the magnetic field. The magnetic field correction method was employed to accurately determine the magnetic properties. The experimental results showed that the magnetic field correction method provided a reliable estimation of the real magnetic field, and thus had a high precision in magnetic properties calculation. Besides, this method performed well even when exposed to weak applied coil magnetic fields. The measurement noise analysis showed that the total calculation errors of the magnetic field correction method were lower than those of the traditional method, and the coils and magnetometers should be installed carefully to reduce the errors in magnetic properties calculation.

In the experiment, only one magnetic dipole and the geomagnetic field were considered to represent the background magnetic field. By modeling the magnetic sources as more dipoles, the magnetic field correction method can be extended to more complex background magnetic fields.

CRediT authorship contribution statement

Binbin Liu: Investigation, Software, Writing – original draft, Visualization. **Zhen Yang:** Investigation, Formal analysis. **Li-e Qiang:** Investigation, Writing – review & editing. **Peng Xu:** Conceptualization, Methodology. **Xiaodong Peng:** Investigation, Resources. **Ziren Luo:** Investigation, Methodology. **Yuzhu Zhang:** Investigation, Writing – original draft. **Wenlin Tang:** Software, Validation.

Declaration of competing interest

The authors declare that they have no known competing financial interests or personal relationships that could have appeared to influence the work reported in this paper.

Data availability

Data will be made available on request.

Acknowledgments

Appendix. The magnetic force

The lowest order force exerted on a localized current distribution in an external magnetic field $\mathbf{B}$ can be written as [33]

$$\mathbf{F} = \nabla(\mathbf{m}_\rho \cdot \mathbf{B}), \tag{21}$$

where $\mathbf{m}_\rho$ is the TM magnetic moment density, and it can be written as

$$\mathbf{m}_\rho = \mathbf{m}_\mathrm{r} + \mathbf{m}_\mathrm{i} = \mathbf{m}_\mathrm{r} + \frac{\chi}{\mu_0}\mathbf{B}, \tag{22}$$

where $\mathbf{m}_\mathrm{r}$ is the remanent magnetization; $\mathbf{m}_\mathrm{i}$ is the induced magnetic moment, which is proportional to the field $\mathbf{B}$. Then, the total force exerted on the TM can be calculated as

$$
\begin{aligned}
\mathbf{F} &= \iiint_{V_{\mathrm{TM}}} \nabla(\mathbf{m}_\rho \cdot \mathbf{B})\, dx\, dy\, dz \\
&= \iiint_{V_{\mathrm{TM}}} \nabla\left[\left(\mathbf{m}_\mathrm{r} + \frac{\chi}{\mu_0}\mathbf{B}\right) \cdot \mathbf{B}\right] dx\, dy\, dz \\
&= \iiint_{V_{\mathrm{TM}}} \left[\left(\left(\mathbf{m}_\mathrm{r} + \frac{\chi}{\mu_0}\mathbf{B}\right) \cdot \nabla\right)\mathbf{B}\right. \\
&\qquad + \left(\mathbf{m}_\mathrm{r} + \frac{\chi}{\mu_0}\mathbf{B}\right) \times (\nabla \times \mathbf{B}) \\
&\qquad + (\mathbf{B} \cdot \nabla)\left(\mathbf{m}_\mathrm{r} + \frac{\chi}{\mu_0}\mathbf{B}\right) \\
&\qquad \left. + \mathbf{B} \times \left(\nabla \times \left(\mathbf{m}_\mathrm{r} + \frac{\chi}{\mu_0}\mathbf{B}\right)\right)\right] dx\, dy\, dz.
\end{aligned}
$$

Considering that $\nabla \times \mathbf{B} = 0$, $\nabla \cdot \mathbf{m}_r = 0$, and $\nabla \times \mathbf{m}_r = 0$, the final magnetic force expression can be written as

$$
\begin{aligned}
\mathbf{F} &= \iiint_{V_{\text{TM}}} \left[\left(\left(\mathbf{m}_r + \frac{\chi}{\mu_0} \mathbf{B} \right) \cdot \nabla \right) \mathbf{B} \right. \\
&\quad \left. + \left(\frac{\chi}{\mu_0} \mathbf{B} \cdot \nabla \right) \mathbf{B} \right] dx\,dy\,dz \\
&= \iiint_{V_{\text{TM}}} \left[\left(\mathbf{m}_r + \frac{2\chi}{\mu_0} \mathbf{B} \right) \cdot \nabla \right] \mathbf{B}\, dx\,dy\,dz.
\end{aligned} \tag{23}
$$

References

[1] Amaro-Seoane P, Audley H, Babak S, Baker J, Barausse E, Bender P, et al. Laser interferometer space antenna. 2017, arXiv preprint arXiv:1702.00786.

[2] Bruinsma S, Tamagnan D, Biancale R. Atmospheric densities derived from CHAMP/STAR accelerometer observations. Planet Space Sci 2004;52(4):297–312.

[3] Tapley BD, Bettadpur S, Watkins M, Reigber C. The gravity recovery and climate experiment: Mission overview and early results. Geophys Res Lett 2004;31(9).

[4] Marque J, Christophe B, Liorzou F, Bodovillé G, Foulon B, Guérard J, et al. The ultra sensitive accelerometers of the ESA GOCE mission. In: 59th international astronautical congress, vol. 137. 2008, p. 2008.

[5] Weber WJ, Cavalleri A, Dolesi R, Fontana G, Hueller M, Vitale S. Position sensors for LISA drag-free control. Classical Quantum Gravity 2002;19(7):1751.

[6] Touboul P, Rodrigues M, Willemenot E, Bernard A. Electrostatic accelerometers for the equivalence principle test in space. Classical Quantum Gravity 1996;13(11A):A67.

[7] Touboul P, Rodrigues M. The MICROSCOPE space mission. Classical Quantum Gravity 2001;18(13):2487.

[8] Pradels G, Touboul P. In-orbit calibration approach of the microscope experiment for the test of the equivalence principle at 10- 15. Classical Quantum Gravity 2003;20(13):2677.

[9] Hudson D, Chhun R, Touboul P. Development status of the differential accelerometer for the MICROSCOPE mission. Adv Space Res 2007;39(2):307–14.

[10] Hu W-R, Wu Y-L. Taiji program in space for gravitational wave physics and nature of gravity. Natl Sci Rev 2017.

[11] Luo Z, Guo Z, Jin G, Wu Y, Hu W. A brief analysis to Taiji: Science and technology. Results Phys 2020;16:102918.

[12] Luo J, Chen L-S, Duan H-Z, Gong Y-G, Hu S, Ji J, et al. TianQin: a space-borne gravitational wave detector. Classical Quantum Gravity 2016;33(3):035010.

[13] Yang F, Hong W, Li H, Ma D. Adaptive charge control for the space inertial sensor. Classical Quantum Gravity 2023;40(7):075004.

[14] Antonucci F, Armano M, Audley H, Auger G, Benedetti M, Binetruy P, et al. From laboratory experiments to LISA pathfinder: achieving LISA geodesic motion. Classical Quantum Gravity 2011;28(9):094002.

[15] Hanson J, Mac Keiser G, Buchman S, Byer R, Lauben D, DeBra D, et al. ST-7 gravitational reference sensor: analysis of magnetic noise sources. Classical Quantum Gravity 2003;20(10):S109.

[16] Diaz-Aguiló M, García-Berro E, Lobo A. Theory and modelling of the magnetic field measurement in LISA PathFinder. Classical Quantum Gravity 2010;27(3):035005.

[17] Hueller M, Armano M, Carbone L, Cavalleri A, Dolesi R, Hoyle C, et al. Measuring the LISA test mass magnetic properties with a torsion pendulum. Classical Quantum Gravity 2005;22(10):S521.

[18] Bender P, et al. Laser interferometer space antenna: A cornerstone mission for the observation of gravitational waves, vol. 11. ESA report no ESA-SCI (2000), 2000.

[19] Keyser PT, Jefferts SR. Magnetic susceptibility of some materials used for apparatus construction (at 295 K). Rev Sci Instrum 1989;60(8):2711–4.

[20] Davis R. New method to measure magnetic susceptibility. Meas Sci Technol 1993;4(2):141.

[21] Franco V, Dodrill B. Magnetic measurement techniques for materials characterization. Springer; 2021.

[22] Yin H, Tan D-Y, Hu M, Wang S, Bai Y-Z, Wu S-C, et al. Measurements of magnetic properties of kilogram-level test masses for gravitational-wave detection using a torsion pendulum. Phys Rev A 2021;15(1):014008.

[23] Quinn T, Speake C, Davis R. Novel torsion balance for the measurement of the Newtonian gravitational constant. Metrologia 1997;34(3):245.

[24] Schlamminger S, Choi K-Y, Wagner TA, Gundlach JH, Adelberger EG. Test of the equivalence principle using a rotating torsion balance. Phys Rev Lett 2008;100(4):041101.

[25] Yan N, Kühnel M, Vasilyan S, Fröhlich T. Torsion balance-based system for high-precision force measurement in horizontal plane: part I. Development concept. Meas Sci Technol 2018;29(8):084001.

[26] Hai-Bo T, Yan-Zheng B, Ze-Bing Z, Yu-Rong L, Jun L. Measurement of magnetic properties of an inertial sensor with a torsion balance. Chin Phys Lett 2009;26(4):040403.

[27] Xu J-H, Liu Q, Luo X, Zhu L, Zhao H-H, Wang Q-L, et al. Measuring ac magnetic susceptibility at low frequencies with a torsion pendulum for gravitational-wave detection. Phys Rev A 2022;18(4):044010.

[28] Carbone L, Cavalleri A, Dolesi R, Hoyle C, Hueller M, Vitale S, et al. Achieving geodetic motion for LISA test masses: ground testing results. Phys Rev Lett 2003;91(15):151101.

[29] Diaz-Aguiló M, Mateos I, Ramos-Castro J, Lobo A, García-Berro E. Design of the magnetic diagnostics unit onboard LISA Pathfinder. Aerosp Sci Technol 2013;26(1):53–9.

[30] Russano G. A torsion pendulum ground test of the LISA Pathfinder free-fall mode. 2016, arXiv preprint arXiv:1609.00002.

[31] Carbone L, Cavalleri A, Dolesi R, Hoyle C, Hueller M, Vitale S, et al. Upper limits on stray force noise for LISA. Classical Quantum Gravity 2004;21(5):S611.

[32] Hueller M, Cavalleri A, Dolesi R, Vitale S, Weber W. Torsion pendulum facility for ground testing of gravitational sensors for LISA. Classical Quantum Gravity 2002;19(7):1757.

[33] Jackson JD. Classical electrodynamics. American Association of Physics Teachers; 1999.

[34] National Geophysical Data Center. NCEI geomagnetic calculators. U.S. Department of Commerce, https://www.ngdc.noaa.gov/geomag/calculators/magcalc.shtml#igrfwmm.

[35] Dufay B, Saez S, Dolabdjian C, Yelon A, Ménard D. Development of a high sensitivity giant magneto-impedance magnetometer: Comparison with a commercial flux-gate. IEEE Trans Magn 2012;49(1):85–8.

[36] Hauser H, Fulmek PL, Haumer P, Vopalensky M, Ripka P. Flipping field and stability in anisotropic magnetoresistive sensors. Sensors Actuators A 2003;106(1–3):121–5.

[37] Mateos I, Diaz-Aguiló M, Gibert F, Lloro I, Lobo A, Nofrarias M, et al. Temperature coefficient improvement for low noise magnetic measurements in LISA. J Phys Conf Ser 2012;363(1):012051.

[38] Mateos I, Diaz-Aguiló M, Gesa L, Gibert F, Karnesis N, Lloro I, et al. Magnetic field measurement using chip-scale magnetometers in eLISA. J Phys Conf Ser 2015;610(1):012028.

[39] Luong V-S, Chang C-H, Jeng J-T, Lu C-C, Hsu J-H, Chang C-R. Reduction of low-frequency noise in tunneling-magnetoresistance sensors with a modulated magnetic shielding. IEEE Trans Magn 2014;50(11):1–4.

[40] Hu M, Bai Y, Zhou Z, Li Z, Luo J. Resonant frequency detection and adjustment method for a capacitive transducer with differential transformer bridge. Rev Sci Instrum 2014;85(5).

[41] Tian W, Wu S, Zhou Z, Qu S, Bai Y, Luo J. High resolution space quartz-flexure accelerometer based on capacitive sensing and electrostatic control technology. Rev Sci Instrum 2012;83(9).

[42] Mateos I, Díaz-Aguiló M, Ramos-Castro J, García-Berro E, Lobo A. Interpolation of the magnetic field at the test masses in eLISA. Classical Quantum Gravity 2015;32(16):165003.

[43] Auster H, Glassmeier K, Magnes W, Aydogar O, Baumjohann W, Constantinescu D, et al. The THEMIS fluxgate magnetometer. Space Sci Rev 2008;141:235–64.